A multi-scale gap-bridging CWE approach to windblown sand action on critical infrastructures: Modelling framework and case study on a high-speed railway line

Journal of Wind Engineering & Industrial Aerodynamics 249 (2024) 105722

Contents lists available at ScienceDirect

Journal of Wind Engineering & Industrial Aerodynamics

journal homepage: www.elsevier.com/locate/jweia

A multi-scale gap-bridging CWE approach to windblown sand action on critical infrastructures: Modelling framework and case study on a high-speed railway line

Manuel Gageik [a], Carlos-José Rodriguez Ahlert [a], Nicolas Coste [b,d], Lorenzo Raffaele [c,d,*]

[a] SIEMENS Mobility GmbH, Duisburger Straße 145, Krefeld, 47829, Germany
[b] Optiflow Company, Chemin de la Madrague-Ville, 160, Marseille, 13015, France
[c] Department of Architecture and Design, Politecnico di Torino, Viale Mattioli 39, Torino, 10126, Italy
[d] Windblown Sand Modeling and Mitigation Joint Research Group, Italy-France

ARTICLE INFO

Keywords:
Multi-scale
Multi-physics
Windblown sand action
Railway aerodynamics
Rolling stock
Computational wind engineering

ABSTRACT

Windblown sand action on critical infrastructures, such as high-speed railway lines, can completely inhibit their operation detrimentally affecting their safety and capacity. Several key components of the infrastructure are affected, among them the rolling stock material and infrastructure equipment. Computational Wind Engineering (CWE) is becoming more and more adopted during the different design stages to assess the impact of windblown sand. However, CWE-based analysis and design remain challenging because of the different scales involved in windblown sand transport starting from the full alignment scale (macro-scale), to the railway body (meso-scale), to the rolling stock (micro-scale). An innovative multi-scale modelling approach is proposed to bridge the gap between macro and micro scales involved in windblown sand processes, allowing to assess windblown sand action on key components. An exploratory case study addressing rolling stock operation in sandy environment along an high-speed railway line is analysed and discussed. This demonstrates the soundness of the approach in identifying most endangered railway segments, railway body sedimentation-prone areas and rolling stock components, and in quantifying windblown sand action at different scales. The proposed approach is well suited also to support the conceptual design of Sand Mitigation Measures.

1. Introduction

Windblown sand action is widely recognized as a key hazard affecting civil structures and infrastructures in sandy environments, such as desert regions and coastal zones (Raffaele and Bruno, 2019). On one hand, desert regions are increasingly hosting human activities and built structures. On the other hand, climate change is progressively inducing the increment of the windstorm frequency, and associated sand transport events from sandy coasts to built-up areas. Within this scenario, critical infrastructures are particularly noteworthy given their social and economical impact.

Critical railway infrastructures in sandy environments are well known to be particularly sensitive to windblown sand, because of their impressive linear extension causing the crossing different geomorphological environments (e.g. Raffaele and Bruno, 2020), and the specific vulnerability of railway components to windblown sand action (Bruno et al., 2018b). The number of critical infrastructure railway projects currently ongoing and planned in sandy regions across North Africa, Middle East, and Southeast Asia is expected to progressively increase in the near future. At the same time, railway infrastructure components are particularly sensitive to windblown sand despite its detrimental effect endangering both safety and serviceability (Bruno et al., 2018b). Windblown sand interacts with any railway infrastructure component inducing sand transport and sedimentation around it. Some non-exhaustive examples of windblown sand effects on railway infrastructures include: railway sand coverage compromising train passengers' safety (e.g. Cheng et al., 2015); ballast contamination and consequent increase of train-induced vibrations and additional damage to superstructure components of the track (e.g. Zakeri et al., 2012); rail grinding and rolling stock wheels profiling induced by the thin sand layer sedimented on the rail-wheel contact interface (e.g. Faccoli et al., 2018); sand impact on high-speed running trains causing the premature wear of train elements and the infiltration in the heating, ventilation and air conditioning system (e.g. Paz et al., 2015).

Windblown sand is a multi-physics process resulting from the interaction of wind flow aerodynamics and sand particles erosion, transport,

* Corresponding author at: Department of Architecture and Design, Politecnico di Torino, Viale Mattioli 39, Torino, 10126, Italy.
E-mail address: lorenzo.raffaele@polito.it (L. Raffaele).

https://doi.org/10.1016/j.jweia.2024.105722
Received 9 January 2024; Received in revised form 22 March 2024; Accepted 10 April 2024
Available online 19 April 2024

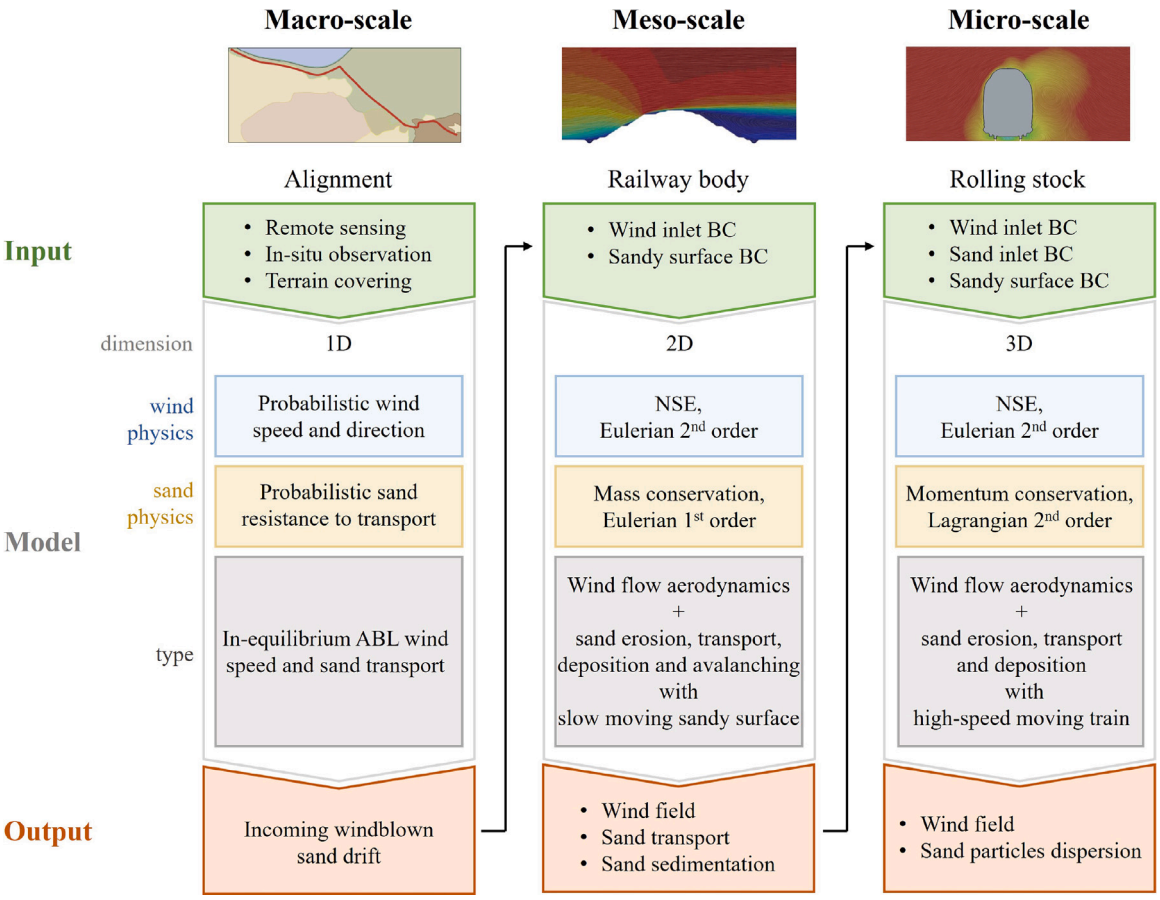

Fig. 1. Multi-scale/multi-physics approach to windblown sand action.

sedimentation and avalanching (e.g. Kok et al., 2012). Windblown sand is also a multi-scale process (e.g. Pye and Tsoar, 2009) ranging from the submillimeter-scale of the single sand grain (micro-scale), to the ten/hundred meters-scale of sand bed forms (meso-scale), to the hundred kilometers-scale of the windblown sand transport at the regional scale (macro-scale). Given the multi-physics/multi-scale nature of the phenomenon and the resulting difficulties arising from its physical modelling through in-field and wind tunnel tests (e.g. Raffaele et al., 2021, 2023), mathematical modelling approaches, properly tuned and validated on the basis of physical testing, are usually preferred in the design practice (e.g. Lo Giudice et al., 2019). Accordingly, windblown sand mathematical modelling is usually compartmentalized into different classes of problems, strictly related to the retained scale of the physical process. In the following, such mathematical modelling approaches are briefly reviewed by referring to the three scales mentioned above.

At the *macro-scale*, windblown sand is usually modelled to ascertain the amount of incoming sand drift. The modelling approach to evaluate sand drift has been first introduced by Fryberger and Dean (1979) and consolidated in several areas of application from geomorphology to coastal and civil engineering (see e.g. Barchyn and Hugenholtz, 2011; Riksen et al., 2016; Cheng et al., 2015). Such a modelling approach mainly consists in semi-empirical analytical expressions evaluating the in-equilibrium sand transport depending on in-equilibrium Atmospheric Boundary Layer (ABL) wind field conditions and sand bed resistance to erosion.

At the *meso-scale*, windblown sand is usually modelled via so-called cellular automaton models and Computational Wind Engineering (CWE) approaches. Cellular automaton models are widespread since they allow to model erosion, transport, and deposition processes as time-dependent stochastic interactions between cells of a lattice (to study e.g. long-term evolution of dune fields Narteau et al., 2009) with reduced computational resources. However, they are unable to model windblown sand transport in air (i.e. they only account for the morphodynamic evolution of the sand bed) and out-of-equilibrium conditions, i.e. sand transport, erosion and sedimentation around any kind of solid obstacle. Therefore, Computational Wind Engineering (CWE) models for fluid-driven particulate transport have considerably increased in the last decades (Lo Giudice et al., 2019). At the meso-scale, fully Eulerian models are usually preferred given their lower computational cost with respect to Eulerian–Lagrangian CWE modelling approaches. Indeed, fully Eulerian models are based on continuum approximations or closures to model erosion, transport, sedimentation, and consequent avalanching determining the morphodynamic evolution of the sand bed (e.g. Lo Giudice and Preziosi, 2020). As such, windblown sand is assessed through the resolution of the Navier–Stokes Equations for the wind flow phase coupled with mass and momentum conservation equations for the dispersed sand phase (Lo Giudice et al., 2019).

At the *micro-scale*, Eulerian–Lagrangian CWE models allow to directly simulate dispersed sand particles preserving the granular nature of sand. Such modelling approaches consist in solving the equations of motion for each particle including collisions, to get individual trajectories. However, the large number of particles considerably limits the size of the domain (Lo Giudice and Preziosi, 2020).

Multi-scale modelling and simulation has recently emerged as one of the focal research areas in applied science and engineering (Fish, 2010). A remarkable pioneering example, albeit in a different field of application, is represented by the multi-scale multi-physics multi-dimensional model by Formaggia et al. (2001), where the multi-scale strategy allows to dramatically reduce computational complexity by coupling detailed 2D/3D simulation modelling the micro/meso-scales with simplified 1D simulation modelling the macro-scale. In the same spirit, the present

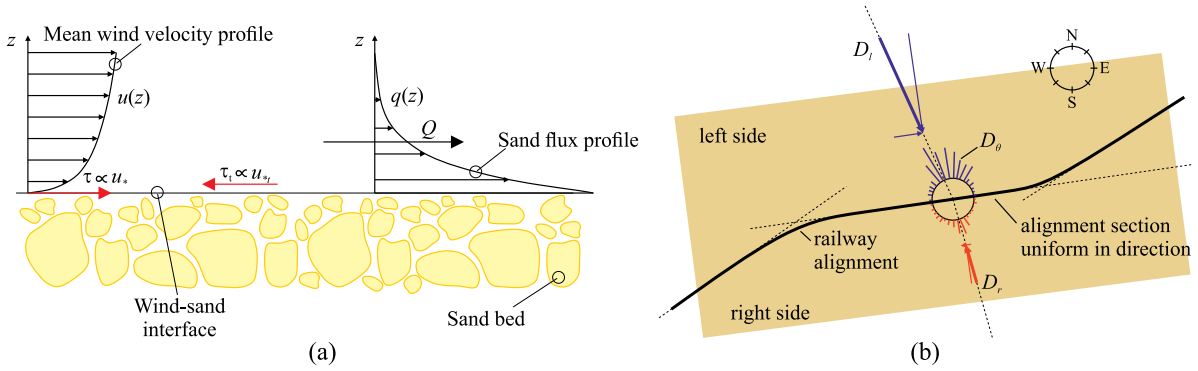

Fig. 2. Wind velocity and sand flux profiles during saltation (a), incoming left-side D_l and right-side D_r sand drift along a generic infrastructure alignment (b).

study proposes a multi-scale CWE approach to windblown sand action taking advantage of the complementarity of the approaches discussed above. In particular, a close and fruitful cooperation between Siemens Mobility (Krefeld, Germany) and Windblown Sand Modelling and Mitigation (WSMM) joint research group (Italy-France) was established to develop a multi-scale modelling framework to assess windblown sand action on the railway track and rolling stock. The proposed multi-scale CWE approach is then applied and tested on an exploratory case study dealing with a desert railway line.

The paper is organized into three further sections. Section 2 showcase the conceived multi-scale modelling framework discussing in detail the adopted methodology, required input and expected output for model adopted, each of them retaining a scale of the problem. Key results are discussed in Section 3. Finally, conclusions and perspectives are outlined in Section 4.

2. Multi-scale modelling framework

This study proposes a novel multi-scale modelling framework to assess windblown sand action on critical infrastructures. In particular, such an approach is applied to a critical High-Speed Railway infrastructure crossing desert environments. The overall modelling framework is summarized in Fig. 1, showing the required *input*, the adopted *model* features, and resulting *output* for each analysed scale. In the following, input, model features, and output are detailed for each analysed scale, i.e. at the hundred kilometers-scale of the whole infrastructure length (macro-scale, Section 2.1), at the hundred meters-scale of the railway body characteristic length (meso-scale, Section 2.2), and at the ten meter-scale of the rolling stock (micro-scale, Section 2.3).

2.1. Macro-scale modelling of incoming sand drift

The incoming windblown sand drift is obtained from the incoming transport rate Q, defined as the volume of sand per crosswind meter per hour carried by the incoming wind undisturbed by any obstacles, in analogy to the incoming mean wind velocity in the wind engineering practice (EN 1991-1-4, 2005). Q results from the integral of the windblown sand saltation flux profile $q(z)$ along the vertical direction z (see Fig. 2a). In practice, Q is usually modelled by means of semi-empirical analytical expressions (Kok et al., 2012), that heuristically account for the features of both the in-equilibrium ABL wind flow and the sand bed. $Q > 0$ occurs $\tau > \tau_t$, where τ is the wind-induced shear stress at the sand bed surface, and τ_t is the sand bed resistance to erosion, i.e. the lower value of the shear stress at which sand grains loose their static equilibrium and saltation occurs (see Fig. 2a). τ is usually replaced by the wind shear velocity $u_* = \sqrt{\tau/\rho}$, where ρ is the air density. In turn, u_* is recovered from the mean wind speed profile for in-equilibrium ABL flow for a given aerodynamic roughness length z_0 as $u_* = 0.41 u_{ref} / \ln\left(z_{ref}/z_0\right)$, where the reference height is adopted as $z_{ref} = 10$ m, and the corresponding wind speed u_{ref} is averaged over 10 min, i.e. the effect of the wind turbulence fluctuations on Q is neglected. Analogously, τ_t is replaced by the so-called threshold shear velocity u_{*t}, expressed empirically as a function of the sand grain mean diameter d (Shao, 2008). It follows that the semi-empirical analytical expression of incoming transport rate take the form $Q = Q\left(u_*, u_{*t}\right)$.

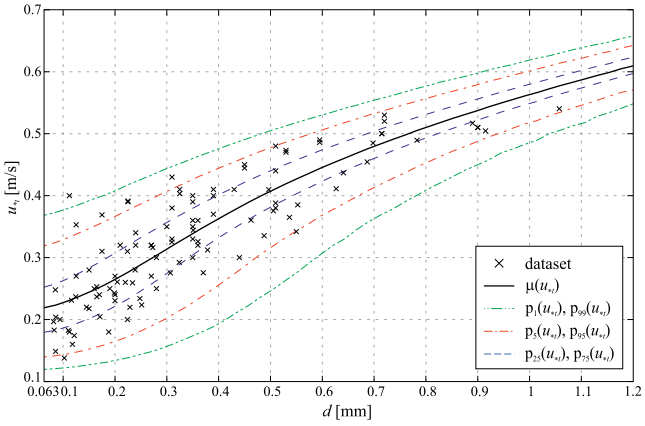

Fig. 3. Threshold shear velocity of natural particles: measurements and copula-based regression, after Raffaele et al. (2016).

It is worth stressing that u_* and u_{*t} are bulk random variables that incorporate the effects of natural phenomena varying in both space and time. As a result, they shall be characterized in statistics terms through remote sensing and/or in-situ measurements. u_{*t} was recently statistically characterized by Raffaele et al. (2016, 2018). In Raffaele et al. (2016), a dataset including 109 d-u_{*t} measurements was collected from previously published studies. Estimates of conditional probability distributions of u_{*t} for given values of d are obtained via copula-based regression so to describe u_{*t} high order statistics. In particular, Fig. 3 shows the d-u_{*t} dataset with mean value (μ) and percentiles (p) curves resulting from Raffaele et al. (2016).

The full probabilistic modelling of Q_θ was provided in Raffaele et al. (2017), where u_{*t} is described by non-parametric kernel distributions, while the wind shear velocity $u_{*,\theta}$ for each incoming wind direction θ is described by hybrid Weibull distribution on the base of available in-site anemometric data. In the light of this, Q_θ is expressed via the semi-empirical law proposed by Lettau and Lettau (1978):

$$\begin{aligned} Q_\theta &= C\sqrt{\frac{d}{d_r}}\frac{\rho}{g}u_{*,\theta}^3\left[1-\frac{u_{*t}}{u_{*,\theta}}\right] \qquad \text{if} \quad u_{*,\theta} > u_{*t}, \\ Q_\theta &= 0 \qquad\qquad\qquad\qquad\qquad\quad \text{if} \quad u_{*,\theta} \le u_{*t}, \end{aligned} \tag{1}$$

where $C = 6.7$ is an empirical constant, $d_r = 0.25$ mm is the reference grain diameter, g is the acceleration of gravity, and $u_{*,\theta}$ and u_{*t} are random variables described by the Probability Density Functions (PDFs) $f(u_{*,\theta})$ and $f(u_{*t}|d)$, respectively.

The directional drift potential D_θ is defined as

$$D_\theta = \frac{1}{\rho_b}\frac{T}{T_r}c\sum_{i=1}^{N_\theta} Q_{\theta,in}\Delta t, \tag{2}$$

where ρ_b is the bulk sand density, T is the reference time, T_r is the recording time, c is a site correction taking into account actual terrain characteristics (e.g. sand source availability, presence of vegetation), Δt is the sampling interval of the wind speed and N_θ corresponds to the number of occurrences of the wind speed along the θ direction. In Eq. (2), N_θ and Q_θ are random variables described by the PDF $f(N_\theta)$ and $f(Q_\theta)$.

Finally, the resultant side drift can be defined for the left (D_l) and right sides (D_r) of the railway infrastructure alignment as the vector sum of the components D_θ (see Fig. 2b) as

$$\begin{aligned} D_l &= \sum_{\theta_a}^{\theta_a+\pi} D_\theta, \\ D_r &= \sum_{\theta_a-\pi}^{\theta_a} D_\theta, \end{aligned} \tag{3}$$

being θ_a the direction of the alignment. Such a splitting of the drift into two components is particularly significant, given the line-like nature of the infrastructure alignment.

2.2. Meso-scale modelling of wind flow and sand transport

The wind flow is modelled as a steady incompressible turbulent flow through Navier–Stokes Equations (NSE). In particular, Reynolds-Average Navier–Stokes (RANS) turbulence modelling is preferred because we focused on the long-term behaviour of sand transport which induces sand erosion and accumulation around the railway body and which occurs on a much larger time scale than that of turbulence. The SST k-ω turbulence model is adopted because of its proven accuracy in simulating wind flow separation around bluff bodies (Menter et al., 2003), such as embankments. The same turbulence model has been validated in Bruno and Fransos (2015) and adopted in Bruno et al. (2018a), Horvat et al. (2020), Horvat et al. (2021), and Raffaele et al. (2022) on the same class of problems, i.e. nominal 2D sharp-edged bluff bodies immersed in a turbulent ABL. The whole set of governing equations reads:

$$\begin{aligned} &\frac{\partial u_i}{\partial x_i} = 0, \\ &u_j\frac{\partial u_i}{\partial x_j} = -\frac{1}{\rho}\frac{\partial p}{\partial x_i} + \frac{\partial}{\partial x_j}\left[\nu\left(\frac{\partial u_i}{\partial x_j}+\frac{\partial u_j}{\partial x_i}\right)\right] - \frac{\partial}{\partial x_j}\left(\overline{u_i' u_j'}\right), \\ &u_i\frac{\partial k}{\partial x_i} = \frac{\partial}{\partial x_i}\left[\left(\sigma_k\nu_t+\nu\right)\frac{\partial k}{\partial x_i}\right] + \tilde{P}_k - \beta^* k\omega, \\ &u_i\frac{\partial \omega}{\partial x_i} = \frac{\partial}{\partial x_i}\left[\left(\sigma_\omega\nu_t+\nu\right)\frac{\partial \omega}{\partial x_i}\right] + \alpha\frac{\omega}{k}P_k - \beta\omega^2 + \left(1-F_1\right)\frac{2\sigma_\omega}{\omega}\frac{\partial k}{\partial x_i}\frac{\partial \omega}{\partial x_i}, \end{aligned} \tag{4}$$

where t is time, p is the average pressure, ν is the air kinematic viscosity, ν_t is the so-called turbulent kinematic viscosity, k is the turbulent kinetic energy, and ω is its specific dissipation rate. The kinetic energy production term $\tilde{P}_k$ is modelled by introducing a production limiter to prevent the build-up of turbulence in stagnation regions, i.e. $\tilde{P}_k = \min\left(P_k, 10\beta^* k\omega\right)$, where $P_k \approx 2\nu_t D_{ij}\frac{\partial u_i}{\partial x_j}$ and D_{ij} is the strain-rate tensor. For the sake of conciseness, the definition of the blending function F_1 and the values of the model main constants β^*, σ_k, σ_ω, α, and β are omitted herein. Interested readers can refer to Menter et al. (2003).

Sand-grain roughness wall functions are adopted because of their wide use in CWE (Blocken et al., 2007) and their proven adequacy from past simulations on the same class of problem (e.g Liu et al., 2011; Bruno and Fransos, 2015). In particular, standard wall functions (Launder and Spalding, 1974) with roughness modification (Cebeci and Bradshaw, 1977) are applied. The equivalent sand-grain roughness height is determined equal to $k_s = 9.793 z_0/C_s$, where $C_s = 0.5$ is the roughness constant.

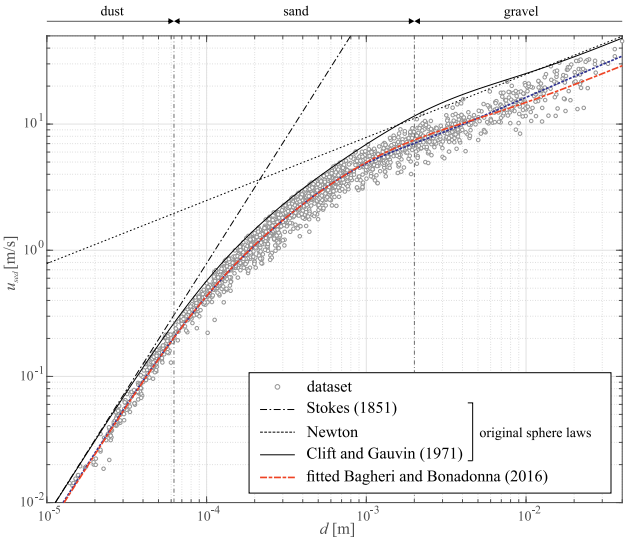

Fig. 4. Sedimentation velocity of natural particles: measurements, original drag laws for spheres, nonlinear regression of law proposed by Bagheri and Bonadonna (2016), after Raffaele et al. (2020).

The transported sand phase is considered as a passive scalar and modelled through the conservation equation of sand volume fraction ϕ_s, where the sand flux is given by the combination of advection by wind, sedimentation induced by gravity, and diffusive flux:

$$\frac{\partial u_{s,i}\phi_s}{\partial x_i} = -u_{sed}\frac{\partial \phi_s}{\partial x_i} - \frac{\partial}{\partial x_i}\left(\nu_{eff}\phi_s\frac{\partial \phi_s}{\partial x_i}\right), \tag{5}$$

where $u_{s,i}$ is the transport velocity of the sand particles by wind taken proportional to u_i, u_{sed} is the vertical sedimentation velocity defined as the maximum velocity a particle attains if falling unhindered in a quiescent fluid of infinite extent, and ν_{eff} takes into account the mixing-diffusive contribution resulting from the combination of ν_t and the viscous effect due to random collisions at the sand surface $\nu_s = A\left(2\sqrt{II_{D_{ij}}}\right)^B$, being A and B model parameters to calibrate the concentration profile and $II_{D_{ij}}$ the second invariant of D_{ij} (Preziosi et al., 2015). u_{sed} results from its full statistical characterization. In Raffaele et al. (2020), 1812 experimental measurements of natural particles sedimentation velocity were recovered from different studies and nonlinear regression was carried out on the consolidated dataset in order to assess the mean value. Fig. 4 shows the $d-u_{sed}$ dataset together with original drag laws for spheres, i.e. the laws by Stokes (1851), Newton (1687) and Clift and Gauvin (1971), and the resulting re-fitted drag law for natural particles proposed by Bagheri and Bonadonna (2016), adopted in this study.

Despite the steady RANS modelling approach, a pseudo-transient approach is adopted to model the very slow morphodynamic evolution of the sand surface induced by erosion and sedimentation and its effect on wind-sand flow field variables. This is accounted for by extrapolating the height $h+\Delta h$ of the wind-sand interface after the time interval Δt by imposing the continuity of sand flux q_i through the wind-sand interface and considering the triggering of avalanching when the sand slope exceeds the critical angle of repose α_{cr}. This leads to the modified

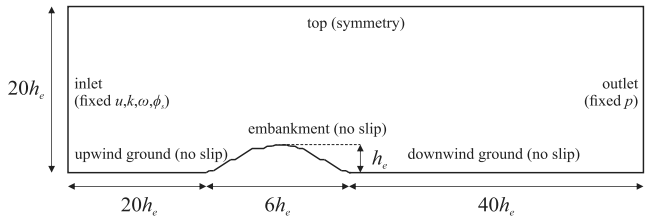

Fig. 5. Scheme of computational domain and BC for meso-scale simulations.

Exner equation (see Lo Giudice and Preziosi, 2020):

$$\frac{\Delta h}{\Delta t} = \nu_{av} \frac{\partial}{\partial x_i} \left[\frac{\left(|\frac{\partial h}{\partial x_i}| - \tan \alpha_{cr} \right)_+}{\sqrt{1 + |\frac{\partial h}{\partial x_i}|^2}} \frac{\frac{\partial h}{\partial x_i}}{|\frac{\partial h}{\partial x_i}|} \right] - \frac{1}{\phi_{cp} - \phi_s} q_i n_i, \tag{6}$$

where the first term represents the wind-sand interface velocity induced by avalanching, being ν_{av} an avalanching diffusion coefficient, while the second term is the wind-sand interface velocity induced by erosion and sedimentation, being ϕ_{cp} the sand close-packing volume ratio and n_i the direction normal to the surface.

The adopted Boundary Conditions (BC) and 2D computational domain is schematically shown in Fig. 5. The railway body cross-section corresponds to the most endangered railway section, i.e. the railway body section for which the incoming sand drift (D_l or D_r) is the highest (see Section 2.1). Null ϕ_s initial conditions are imposed in the whole domain. No-slip BC are imposed at the solid walls. At the inlet, Neumann zero-gradient BC is imposed for p, while Dirichlet BC is imposed on u, k, and ω. At the outlet, Neumann zero-gradient BC is imposed for all flow variables, except for Dirichlet BC for p. At the inlet, a log-law u profile is set according to the 95th percentile of the reference wind speed incoming to the most endangered railway section. The profiles of k and ω are set in accordance to Richards and Norris (2011) to replicate a neutral ABL. Symmetry BC is imposed at the top. Finally, a Dirichlet sand erosion BC is set to properly model erosion on sandy surfaces when $u_* > u_{*t}$, while a Neumann BC is imposed on non-erodible surface (see Ho et al., 2011):

$$-\nu_{eff} \phi_s \frac{\partial \phi_s}{\partial x_i} n_i = A_H \rho \sqrt{\frac{\bar{d}}{g}} \left(u_*^2 - \hat{u}_{*t}^2 \right)_+, \tag{7}$$

where A_H is a model constant, $\bar{d}$ is the mean sand diameter, and $\hat{u}_{*t}$ directly follows from u_{*t} and takes into account the local effect due to slope angle α (see Iversen and Rasmussen, 1994). The computational domain sizes schematized in Fig. 5 are set in order to avoid improper effects of the boundary conditions on the local flow around the embankment (Bruno et al., 2023). The resulting blockage ratio is equal to 5%, in agreement with wind tunnel testing requirements.

Space discretization follows a predominantly structured grid of hexahedral control volumes, with a total number of cells equal to about 5.2e+5. The mesh is refined close to the ground, so that the height n_w of the wall-adjacent cell (i) provides a sufficiently high mesh resolution along the normal direction to the surface in order to adequately resolve the gradients of wind-sand state variables, and (ii) complies with the wall function requirement on dimensionless wall unit $30 < n^+ = n_p u_* / \nu < 200$, being $n_p = n_w/2$ the cell centre height, by setting an average height $n_w = 1.5$ cm.

The cell centre values of the state variables are interpolated at face locations using the second-order central difference scheme for the diffusive terms. The convection terms are discretized by means of the so-called limited linear scheme. A 2nd order accurate bounded total variational diminishing scheme resulting from the application of the (Sweby, 1984) limiter to the central differencing in order to enforce a monotonicity criterion. SIMPLE algorithm is used for pressure–velocity coupling. The meso-scale modelling of wind flow and sand transport is carried out through the Finite Volume open source code OpenFOAM©. On average, a CPU time of about 4 h is required for each steady simulation carried out on the analysed railway body cross-section for successive extrapolated sedimentation levels on Intel(R) Core(TM) dual-processor Sandy Bridge server @ 2.60 GHz with 16 cores employed.

2.3. Modelling of wind flow and sand transport at micro-scale

The wind flow is modelled as a steady incompressible turbulent flow through RANS equations with Realizable k-ε Two-Layer turbulence model (Rodi, 1991; Shih et al., 1994). Such a discrepancy in the adopted turbulence model with respect to meso-scale modelling (Section 2.2) mainly results from the different class of problem which the specific application belongs to. The class of problem mainly depends on the incoming wind features, aerodynamic behaviour of the obstacle, focus of the analysis, and analysis stage (Bruno et al., 2023). In this study, meso-scale and micro-scale approaches mainly differ by the mechanism responsible for wind flow separation. At the meso-scale, wind flow separation around embankment and rails is mainly induced by sharp-edged geometry while, at micro-scale, separation around the rolling stock is mainly induced by Reynolds number and turbulence effect. The same turbulence model has been validated in Ali et al. (2016) on the same class of problems, i.e. smooth rolling stock bluff bodies immersed in a turbulent ABL, and it complies with European standard on train aerodynamics (EN 14067-6, 2018). The adopted turbulence model reads:

$$\begin{aligned} u_i \frac{\partial k}{\partial x_i} &= \frac{\partial}{\partial x_i} \left[\left(\sigma_k \nu_t + \nu \right) \frac{\partial k}{\partial x_i} \right] + P_k - \varepsilon, \\ u_i \frac{\partial \varepsilon}{\partial x_i} &= \frac{\partial}{\partial x_i} \left[\left(\sigma_\varepsilon \nu_t + \nu \right) \frac{\partial \varepsilon}{\partial x_i} \right] + \frac{\varepsilon}{k} C_{\varepsilon 1} P_\varepsilon - C_{\varepsilon 2} \frac{\varepsilon^2}{k + \sqrt{\nu \varepsilon}}, \end{aligned} \tag{8}$$

where ε is the turbulent kinetic energy dissipation rate, P_ε is the ε production term, $C_{\varepsilon 1}$ and $C_{\varepsilon 2}$ are model constants.

The sand phase is modelled through the Lagrange Multiphase Method (LMP), i.e. equations of motion are solved for representative parcels of the dispersed phase instead of tracking each sand particle. This makes LMP, less computationally expensive with respect to traditional Discrete Particle Methods (DPM). Furthermore, LMP is well suited for cases where the volume fraction of the dispersed phase is relatively small, i.e. the motion is dominated by interaction with the continuous phase (one or two-way coupling) rather than interaction with other particles (four-way coupling), and where interaction with solid walls in not negligible. The coupling between wind and sand phases is modelled as one-way, i.e. sand particles are assumed to do not affect the wind phase and each other. In particular, parcels of sand particles are tracked by solving the Lagrangian conservation equations:

$$m_p \frac{\mathrm{d}\mathbf{u}_p}{\mathrm{d}t} = \mathbf{F}_g + \mathbf{F}_d + \mathbf{F}_p + \mathbf{F}_l, \tag{9}$$

where m_p is the particle mass, $\mathbf{u}_p$ is the particle velocity, $\mathbf{F}_g$ is the force induced by gravity, $\mathbf{F}_d$ is the particle drag force, $\mathbf{F}_p$ is the pressure gradient force, and $\mathbf{F}_l$ is the shear lift force. The particle drag force is given by

$$\mathbf{F}_d = \frac{1}{8} \pi d^2 C_d \left| \mathbf{u} - \mathbf{u}_p \right| \left(\mathbf{u} - \mathbf{u}_p \right), \tag{10}$$

where C_d is the drag coefficient. Several laws have been proposed for C_d of natural particles in order to fit experimental data (see e.g. Kang and Liejin, 2006; Lopes et al., 2013). Similarly to the sedimentation velocity of natural particles in Section 2.2, the authors adopted the statistical characterization of C_d of natural particles proposed by Raffaele et al. (2020).

Fig. 6 shows the same dataset included in Fig. 4 mapped on the Re-C_d plane, with original drag laws for spheres, i.e. the laws by Stokes (1851) with $C_d = 24/Re$, Newton (1687) with $C_d \approx 0.46$, and Clift

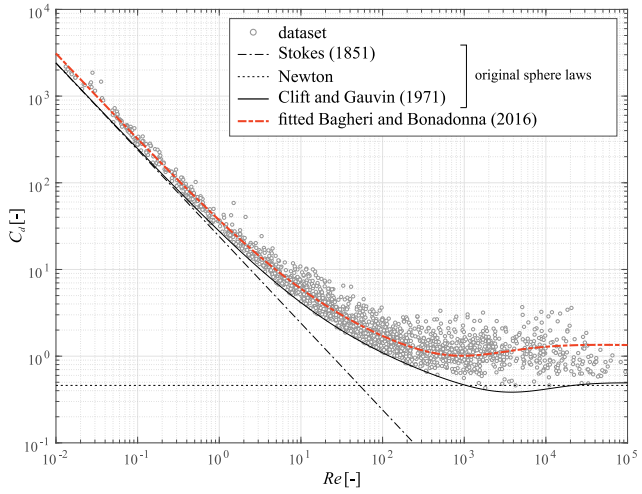

Fig. 6. Drag coefficient of natural particles: measurements, original drag laws for spheres, nonlinear regression of law proposed by Bagheri and Bonadonna (2016), after Raffaele et al. (2020).

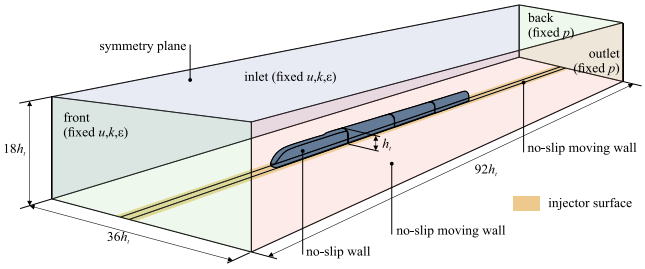

Fig. 7. Scheme of computational domain and BC for micro-scale simulations.

and Gauvin (1971), together with the re-fitted Re-C_d law for natural particles proposed by Bagheri and Bonadonna (2016), adopted in this study. The force induced by the pressure gradient is defined as $\mathbf{F}_p = -m_p/\rho_s \nabla p$, where ρ_s is the sand particle density and ∇p is the gradient of the static pressure. The shear lift force is induced by the wind velocity gradient orthogonal to the particle relative motion and it can be expressed as the Saffman Lift force $\mathbf{F}_l = 1/8\pi d^3 \rho C_{ls}[(\mathbf{u}-\mathbf{u}_p)\times(\nabla\times\mathbf{u})]$ where C_{ls} is the Saffman lift (Saffman, 1965).

Sand particles are affected by the wind instantaneous velocity field, given by the sum of the mean velocity field from RANS and the fluctuating component. As a result, particles dispersion induced by fluctuating fluid forces in time and space needs to be modelled by synthesizing the turbulent wind velocity field. In this study, this is done via a random walk technique adopting the turbulent dispersion model proposed by Gosman and Loannides (1983), in which the random fluctuating component has a Gaussian distribution with zero mean value and standard deviation given by the eddy velocity scale $\sqrt{2k/3}$.

The adopted BC and 3D computational domain are schematically shown in Fig. 7. At the inlet, Dirichlet BC is imposed for u, k, ε according the output of the meso-scale simulation, while Neumann zero-gradient BC is imposed for p. At the outlet, Neumann zero-gradient BC is imposed for all flow variables, except for Dirichlet BC for p. To simulate the rolling stock motion, at the front, Dirichlet BC is imposed for u, k, ε, while at the back, Dirichlet BC is imposed for p. Then, moving no-slip BC are imposed at the ground and track to simulate train speed. Train boundaries are modelled as no-slip BC while top is a symmetry plane. Morphodynamic changes induced by sand erosion and sedimentation are not accounted for in micro-scale simulation. Conversely, sand bed morphodynamics resulting from meso-scale simulations (Section 2.2) is considered to assess the location of sand particles injection surfaces. Particles injection rate is set in accordance to the erosion law proposed by Nickling (1988), due to the shear velocity induced by the rolling stock motion. Finally, rebound of the particles at the solid walls is modelled via the setting of normal and tangential restitution coefficients. The computational domain sizes are set in agreement with the standard (EN 14067-6, 2018), the upwind and downwind fetch distances are set equal to about $17h_t$, being h_t the rolling stock height, while the height of the domain is set equal to $18h_t$ resulting in a blockage ratio equal to 1%. Computational domain sizes are summarized in Fig. 7.

Space discretization and numerical discretization schemes follows the same rationale of meso-scale simulations (see Section 2.2). The height of the wall-adjacent cells is set equal to $n_w = 1.5$ mm. The total number of cells is equal to about 730 millions. The Finite Volume code Simcenter STAR-CCM+© is adopted. A CPU time of about 24 h is required for each simulation on a cluster with 512 cores employed.

3. Application and results

The proposed multi-scale approach in applied to an exploratory case study to demonstrate the technical feasibility in an engineering analysis and design perspective. The showcased application refers to a critical high-speed desert railway infrastructure.

The analysed railway alignment mainly develops along the SouthEast-NorthWest direction, and crosses four main geomorphological zones (see Fig. 8a): a mountainous arid zone, a vegetated/urbanized area, arid-sandy plains, and a coastal zone. Conversely, the alignment is not directly endangered by dune fields. The collected sand samples along the alignment consist of medium sized, well sorted quartz grains. The mean sand grain diameter resulting from the granulometry analysis of the samples is equal to $\bar{d} = 0.21$ mm. The sand loose bulk density, and particle density resulted equal to $\rho_b = 1617$ kg/m^3 and $\rho = 2540$ kg/m^3, respectively.

The adopted regional wind speed dataset refers to the wind velocity field at macro-scale simulated by ERA5 reanalysis (Hersbach et al., 2020). The ERA5 reanalysis combines model data with in-site observations into a complete and consistent dataset. This allows to obtain wind speed data all along the alignment by taking into account the effect of the actual topography surrounding it. In particular, the retained dataset spans from Jan 2010 to Dec 2021 with a time sampling $\Delta t = 1$ h. Wind speed direction is classified into 36 sectors with a sampling yaw angle $\Delta\theta = 10°$. The aerodynamic roughness in proximity of the alignment is set equal to $z_0 = 5\text{e}{-3}$ m, a common value for arid/sandy desert terrains (see e.g. Raffaele et al., 2017). The whole railway alignment is divided into 95 segments as uniform as possible in direction so to relate each segment to a constant value of wind speed magnitude and direction.

The wind rose of each segment is constructed starting form ERA5 data, then classic Weibull PDFs are fit to time series for each wind direction sector $\Delta\theta$. Fig. 8(b, c) collect main synthetic results derived from wind velocity statistical characterization along the railway alignment cumulative length s. Fig. 8(b) shows the maximum value of the wind speed mean μ and 95th percentile p_{95} among the wind directions related to left and right sides of the alignment. The strong wind speed variability in time and space results in the significant gap between $\mu(u)$ and $p_{95}(u)$ curves and their variability along the alignment. In particular, wind speed slightly increases versus s, i.e. it is larger closer to the coast due to the occurrence of strong coastal winds. According to Fig. 8(b, c), winds incoming from the right side of the alignment are in average about 0.9 times lower in p_{95} magnitude but they are nearly 3 times more likely to occur than winds incoming from the left side. This hints the general higher susceptibility of the infrastructure to windblown sand transport incoming from the right side of the alignment.

The statistical description on wind speed and threshold shear velocity are then combined via Eqs. (1), (2) and (3) to define the resultant

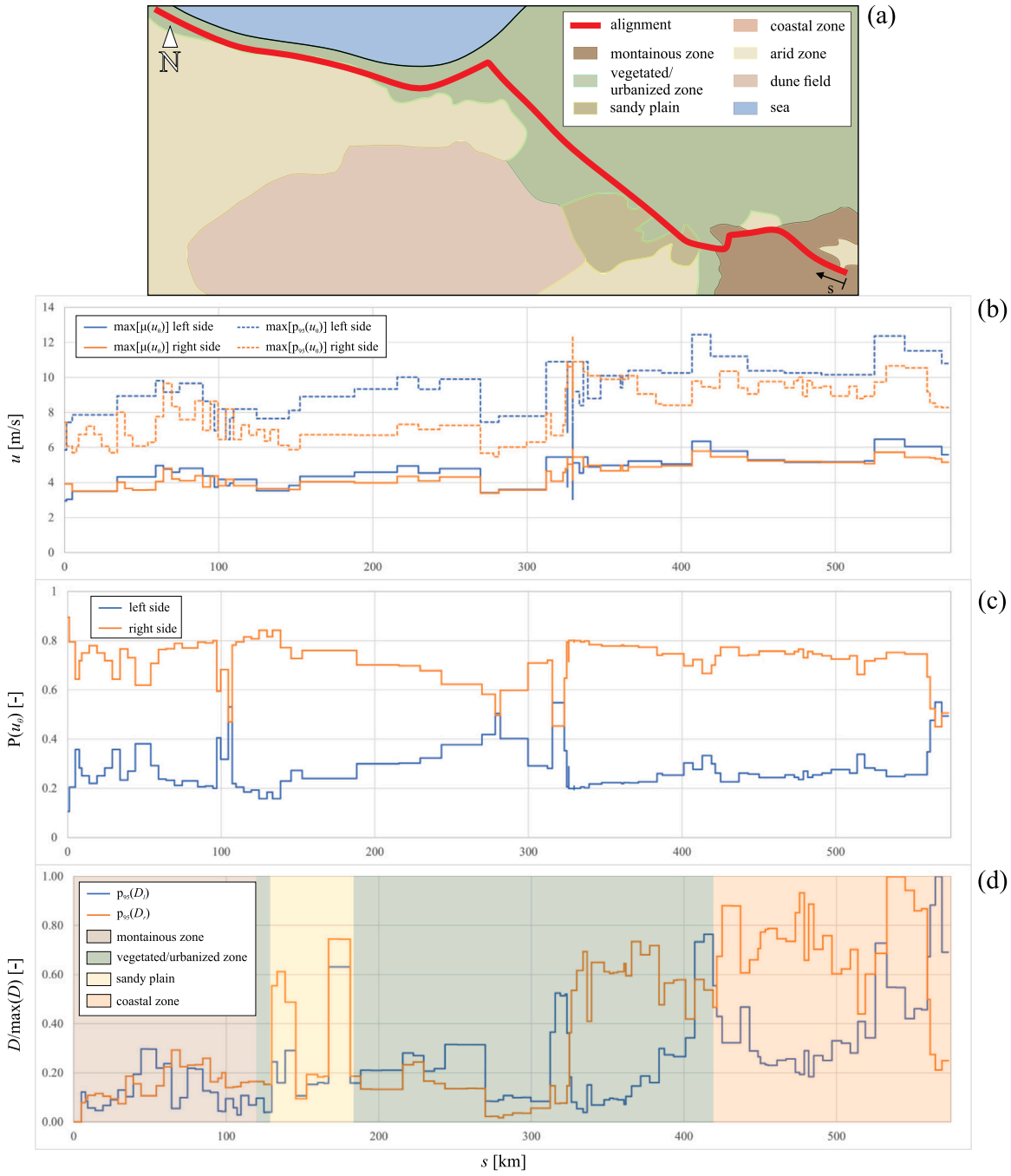

Fig. 8. Sand drift assessment along the railway alignment: sketch of the alignment with geomorphological zones identified in the region (a), incoming wind speed statistics (b), incoming wind occurrence (c), incoming sand drift (d) on left and right sides along the alignment cumulative length.

sand drift for left D_l and right D_r sides of the alignment by means of Monte Carlo method. Fig. 8(d) plots the normalized values of $p_{95}(D_l)$ and $p_{95}(D_r)$ versus the alignment cumulative length s. The portions of the alignment crossing mountainous arid zone, sandy plain, vegetated/urbanized zone, and coastal zone are highlighted in agreement with Fig. 8(a). In particular, it appears that right-side and left-side sand drifts are the lowest in mountainous arid and vegetated/urbanized zones (given the scarce sand covering and presence of vegetation), while they increase (particularly the right side component) in proximity of the sandy plain, because of the larger sand covering, and along the coastal zone, because of the higher wind speed magnitude. The s-wise evaluation of the sand drift allows to identify the location and the yearly incoming transported sand mass for the most endangered railway segments. For analysed case study, such segments are identified within the coastal zone, characterized by stronger winds.

The wind flow features around the railway body referring to the most endangered segments are characterized though a steady RANS simulation. The incoming wind flow reflects actual in-site conditions. The incoming wind speed profile is set according to z_0 = 5e−3 m and $p_{95}(u_*)$ related to the most endangered segment, so as to induce incoming windblown sand transport. Wind speed is assumed perpendicular to the alignment in order to simulate the most severe condition (Horvat et al., 2021). The reference wind speed at the top of the embankment results equal to u_{h_e} = 6 m/s and the corresponding Reynolds number results equal to $\mathrm{Re}_{he} = 5e + 6$. Such a value, together with the railway embankment sharp-edge geometry, suggests that the flow is within the Reynolds super-critical regime, i.e. significant Reynolds effects are not

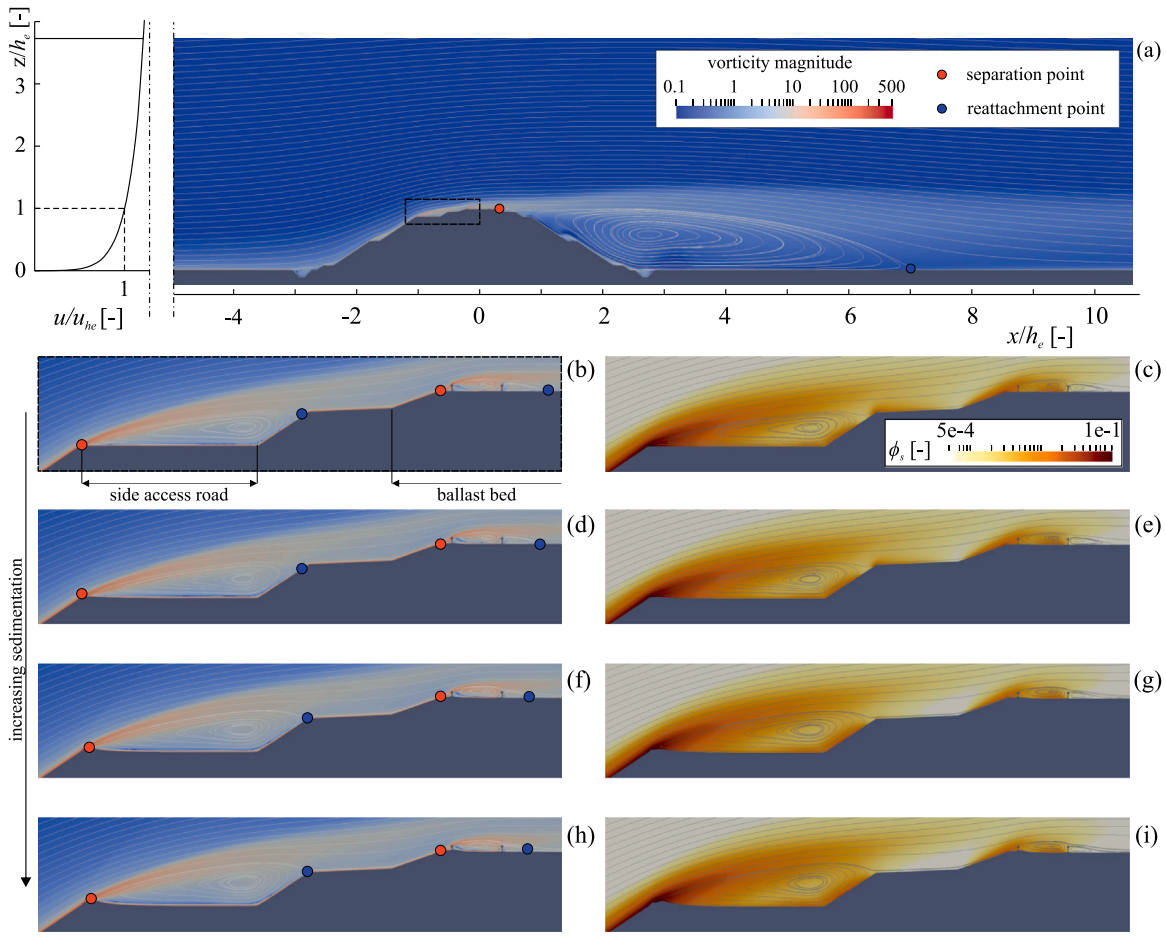

Fig. 9. Wind flow pattern around the clean railway body (a), wind flow pattern (b, d, f, h) and sand concentration (c, e, g, i) around the railway body for successive sedimentation levels.

expected to take place. The sand diameter is set equal to $\bar{d}$ resulting from granulometry analysis. The corresponding mean values of threshold shear velocity and sedimentation velocity are respectively set equal to $u_{*t} = 0.27$ m/s and $u_{sed} = 1.18$ m/s according to the statistical characterizations proposed in Raffaele et al. (2016, 2020). Remaining model constants are set in accordance to Raffaele et al. (2022).

Fig. 9(a) shows the wind flow topology around the clean embankment by means of streamlines coupled with vorticity magnitude field. Upwind the embankment, the vorticity magnitude is high close to the wall due to the ABL, whereas the outer free flow is quasi-irrotational. The boundary layer separates at the downwind sharp edge of the ballast bed at $x/h_e \approx 0.3$, inducing a large clockwise vortex in the wake of the embankment. The wind flow then reattaches at $x/h_e \approx 7$ and accelerates downwind.

To assess the meso-scale sedimentation around the railway body, pseudo-transient simulations are carried out starting from the above-mentioned pure wind flow initial condition. The whole problem is decomposed into consecutive simulations to assess sand transport and the morphodynamic evolution of the sand bed. For each tested sand level: (i) a steady simulation is carried out by assuring the convergence of sand transport, (ii) a new geometry corresponding to a new extrapolated sand level is obtained by shifting the wind-sand interface proportionally to the local value of the erosion-deposition velocity v_{Σ}^{ED}, and (iii) the new geometry is re-meshed. The above steps are repeated systematically in analogy to the procedure reported in Raffaele et al. (2022). In particular, four consecutive simulations have been carried out to describe the morphodynamic evolution of the sand bed, starting from the clean embankment in Fig. 9(b, c) up to the last simulated sand sedimentation level in Fig. 9(h, i).

Fig. 9(b, d, f, h) show a close-up view of the wind flow topology around the side access road and upwind track by means of streamlines coupled with vorticity magnitude field, while Fig. 9(c, e, g, i) show the same window of the domain through wind flow streamlines coupled with dimensionless sand volume fraction field ϕ, for increasing sedimentation levels. Wind flow up over the embankment slopes and detaches wherever it encounters a sharp edge, e.g. in correspondence of the upwind edges of the side access road and ballast bed, giving rise to small recirculation zones. Wind flow vorticity magnitude is higher in correspondence of the shear flow arising from recirculation regions. Sand is eroded upwind the embankment and climbs over the embankment upwind slope. From Fig. 9(c, e, g, i), it emerges how sand erosion is higher where the embankment slope is higher, i.e. where the wind flow accelerate giving rise to high u_*. Sand sediments along the slopes upwind feet and platforms where the wind speed encounters deceleration induced by flow separation. As a result, sand gradually sediments over the side access road and over the ballast bed starting from the separation points. Backward sand erosion also occurs within recirculation regions as highlighted in Horvat et al. (2021). Concerning the side access road, sand sedimentation very slightly moves the position of the reattachment point downwind, without drastically modifying the shape and the size of the recirculation region. This is also testified by the fields of ϕ_s that do not sensibly change as a function of the sedimentation level, form Fig. 9(c) to Fig. 9(i).

Windblown sand flow around the upwind railway track is shown in detail in Fig. 10 through a close-up view of the wind flow velocity coupled with streamlines (in left column) and sand concentration (in right column) for increasing sand sedimentation levels. Three main local clockwise coherent structures develop around the railway track: (i) the

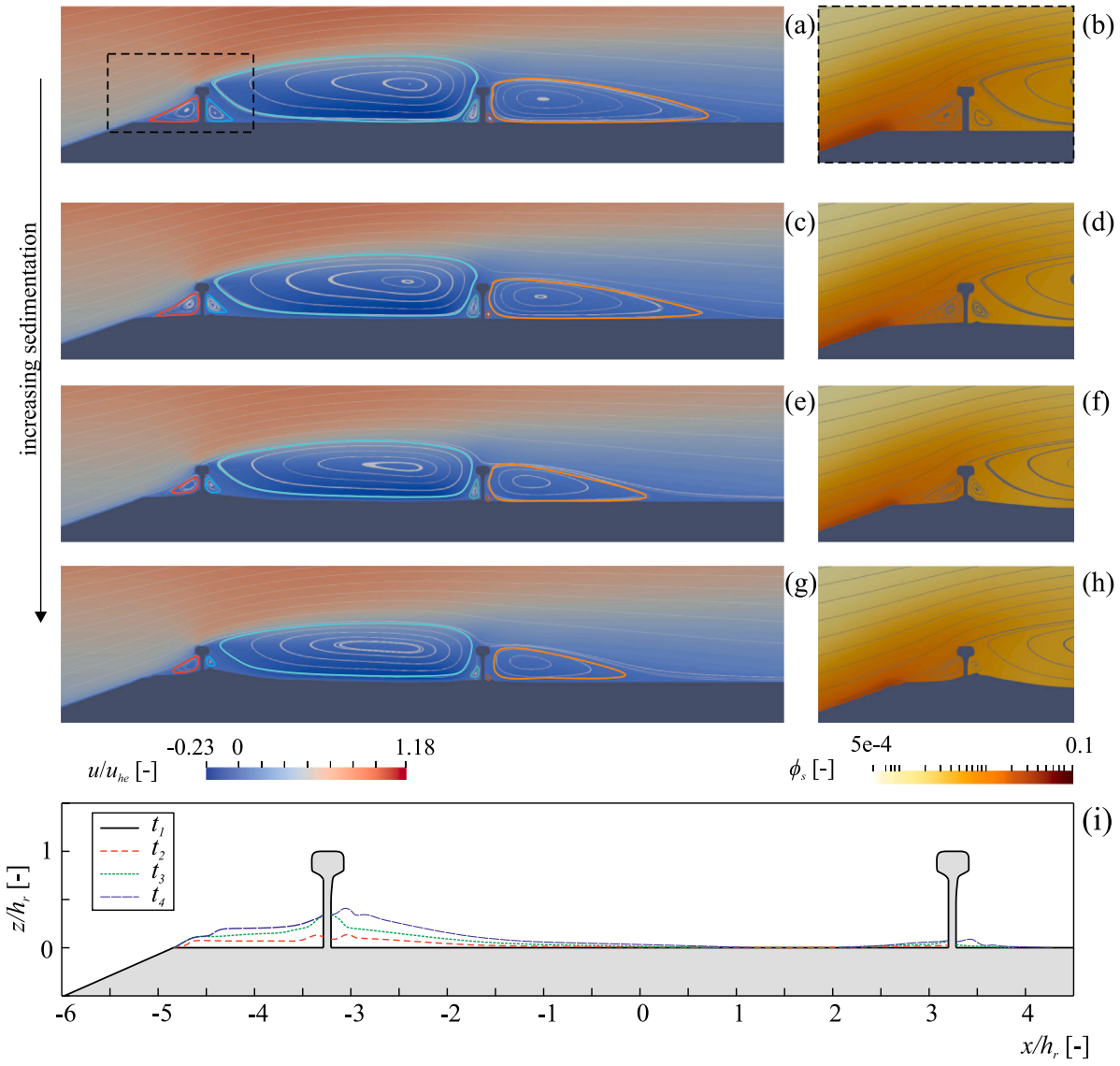

Fig. 10. Wind flow pattern (a, c, e, g) and sand concentration (b, d, f, h) around the upwind railway track for successive sedimentation levels (i).

upwind local vortex (in red), positioned upwind the upwind rail; (ii) the middle local vortex (in cyan), spanning the whole gauge; (iii) the downwind local vortex (in orange), located downwind the downwind rail. Furthermore, additional secondary smaller counter-clockwise vortices appear upwind and downwind each rail. For increasing sedimentation levels, all vortices progressively shrink, suggesting that sand sedimentation will occur up the complete covering of the railway track and the achievement of in-equilibrium sand transport conditions (Raffaele et al., 2021).

Over the ballast bed surface, both erosion and sedimentation processes can be identified. The ballast upwind sharp edge is eroded, because of the wind speedup. Conversely, within main recirculation zones, sedimentation and backwards erosion take place, depending on the streamline curvature close to the wall. Sand sedimentation mainly occurs around the upwind rail. Sand transport and progressive sedimentation around the upwind rail is shown in the close-up views in Fig. 10(b, d, f, h). The progressive sedimentation upwind the rail shrinks the upwind vortex. Part of the eroded sand is transported downwind the upwind rail, entering in the middle local vortex. Similarly, the progressive sedimentation within the rail gauge shrinks the secondary vortex downwind the rail.

Corresponding sedimentation levels are then plotted in Fig. 10(i) for each simulated case. It clearly emerge how the vast majority of the sand start sedimenting upwind and close downwind the upwind rail. Conversely, a small amount of sand sediments around the downwind rail, since the upwind rail traps the vast majority of the incoming sand transport. Of course, the volume of sedimented sand increases progressively from t_1 to t_4. However, the shape of the profile of the sand bed appears to progressively converge to equilibrium conditions, in agreement with Raffaele et al. (2021).

The wind flow and sand transport around the rolling stock are characterized through RANS simulation coupled with LMP for the sand phase. The incoming crosswind flow results from the local wind field simulated at the meso-scale, i.e. it is related to the most endangered railway segments. Sand particles are injected into the domain below the rolling stock in correspondence of the sedimentation zones occurring around the track. The sand particles diameters are set in accordance with the granulometry distribution measured in-site. In particular, particles in the range $d \in [0.02, 0.4]$ mm are considered. The corresponding mean values of the sedimentation velocity are set according to Raffaele et al. (2020). The simulated rolling stock has a height is equal to h_t = 4.15 m. The relative train speed is set equal to v = 63.89 m/s as the maximum train speed under operating conditions.

Fig. 11(a) shows the crosswind flow topology around the clean rolling stock by means of Line Integral Convolution coupled with velocity magnitude field. Part of the incoming crosswind flow is deflected

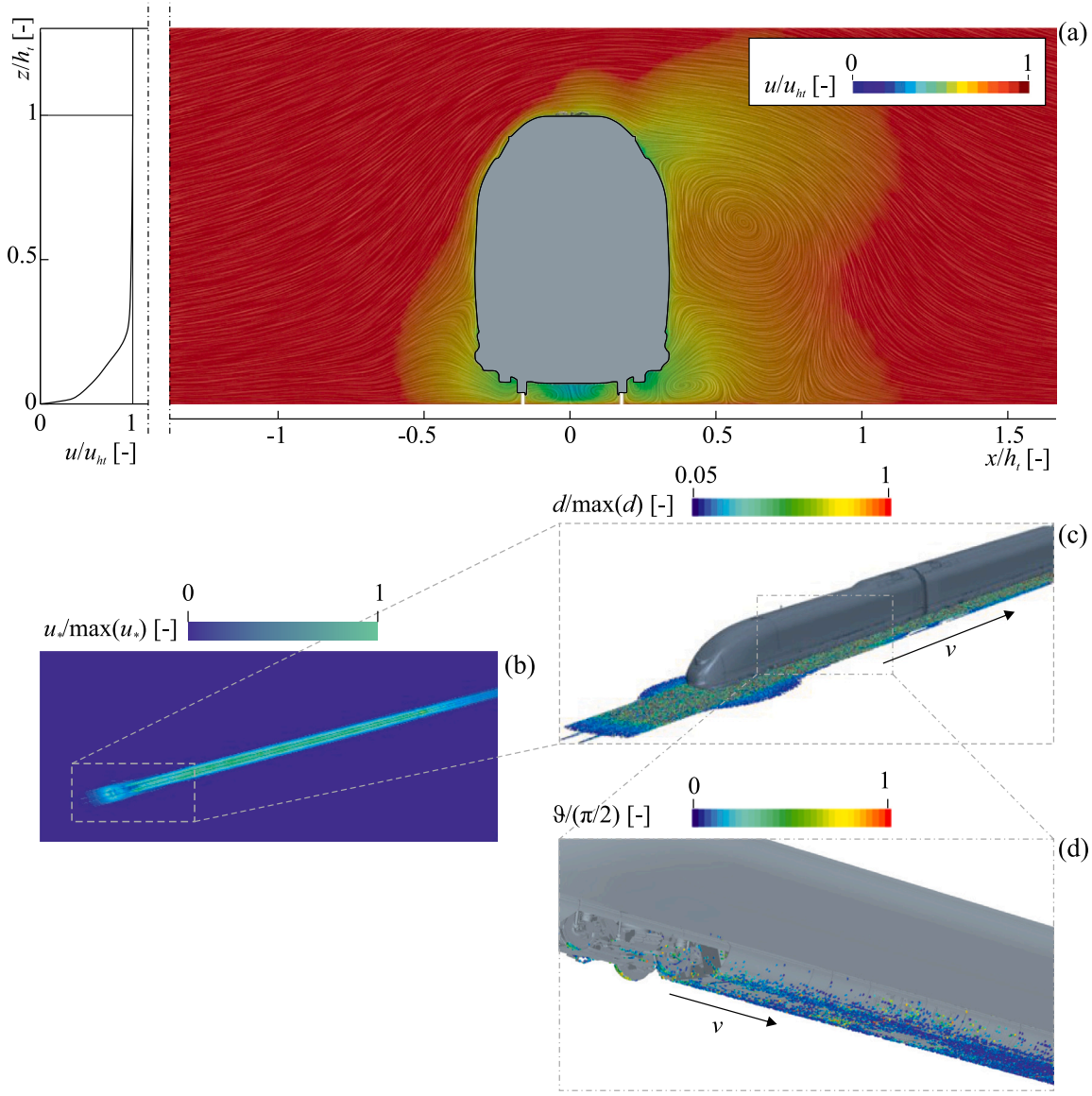

Fig. 11. Windblown sand transport around the rolling stock: crosswind flow pattern around the rolling stock (a), wind shear velocity at ground (b) and sand particles lifting induced by rolling stock motion (c), sand particles impact around the rolling stock (d).

upwards the rolling stock, it remains attached over the roof of the train, then it separates on the downwind side giving rise to a strong downwind vortex spanning about $0.5h_t$. The incoming crosswind flow in the underfloor area is deviated downwards, it passes below the train floor, and in-between the rails developing coherent structures spanning the whole gauge characterized by the coalescence of two counter-rotating vortices. Finally, coherent structures also occurs downwind the downwind rail because of the interaction of the strong downwind vortex, the crosswind flow passing below the train, and the relative wind speed induced by the rolling stock motion.

Sand particles injection surfaces are identified by evaluating the wind shear velocity induced by the passage of the train. Indeed, the relative wind speed induced by the rolling stock motion in the underfloor area induces u_* values much larger than the threshold. In particular, sand particles are injected in correspondence of the surface of the domain where $u_* > u_{*t}$. The injector surface and injected particles are represented in Fig. 11(b, c). It appears how particles with large d are mainly injected where u_* is higher, i.e. in the core of the injector surface. Conversely, at the boundaries of the injector surface, where u_* is lower, most of the injected particles have small values of d. Sand particles are then entrained by high wind shear velocity resulting at ground induced by the train speed v. In particular, Fig. 11(d) shows the amount and the impacting angle ϑ of sand particles hitting a portion of the simulated rolling stock. Most of the sand particles impacts the rolling stock in the underfloor area with a small angle $\vartheta \approx 0$, due to the train relative velocity v and their trajectories following the coherent structures occurring within the underfloor area. Entrained particles progressively rise in height moving to the rear of the train, they are transported crosswind towards the downwind side of the train, and they are consequently lifted from the strong downwind clockwise vortex shown in Fig. 11(a). Such an aerodynamic working principle may cause particles of small diameter to reach the train roof. Such a behaviour could be demanding for the heating, ventilation and air conditioning system, normally installed over the train roof. Indeed, sand particles may infiltrate preventing its correct operation and the health of the coaches environment (Sim et al., 2018). As a result, Receiver SMMs shall be properly designed to mitigate sand particles transport around the coaches for the correct operation of high-speed trains in sandy environments.

Within this framework, the proposed multi-scale CWE approach is well suited not only within the windblown sand transport analysis

stage, i.e. the pure assessment of the windblown sand action, but also within the Sand Mitigation Measure (SMM) design stage.

Indeed, the CWE approach is well suited to sample the wide design space given its flexibility, accuracy, and relative cheapness with respect to in-situ and wind tunnel performance assessment of different SMM design solutions. SMM design solutions, have been categorized into Source, Path and Receiver SMMs in Bruno et al. (2018b), with each category aiming at mitigating a particular windblown sand transport scale. In this framework, Source and Path SMMs are intended to stop the vast majority of the incoming sand drift at macro-scale and meso-scale, respectively. This allows to provide manageable working conditions for complementary Receiver SMMs. Receiver SMMs are then intended to deal with the filtered, low magnitude micro-scale sand drift affecting e.g. rolling stock components (see e.g. the sand-resistant solution proposed in Faccoli et al., 2018), or point-wise sand-sensitive track components such as signalling devices or turnouts (see e.g. the aerodynamic-based solution proposed in Horvat et al., 2022).

4. Conclusion

The present study aims at bridging the existing gaps between different scales in windblown sand transport assessment by proposing a novel multi-scale multi-physics approach to windblown sand action applied on critical high-speed railway infrastructures.

Windblown sand transport is assessed starting from the largest scale of transport. At the macro-scale, in-equilibrium ABL wind flow and sand threshold velocity are defined through one-dimensional analytical models. The wind velocity is defined in probabilistic terms in both direction and magnitude, while sand physics is simply taken into account in terms of sand bed resistance to erosion through the statistical characterization of the particles threshold shear velocity. The resulting probabilistic windblown sand drift allows to identify the most endangered railway segments as the ones located in proximity of the coast because of the strong coastal winds with high probability of occurrence from the right side, while the statistical characterization of incoming wind speed and threshold shear velocity allow to properly set inlet and sand bed erosion boundary conditions as input for the following meso-scale simulations.

At the meso-scale, sand erosion, transport, sedimentation and avalanching are modelled by means of two-dimensional fully-Eulerian computational simulations coupling wind aerodynamics and sand particle transport. Wind phase is modelled by adopting RANS turbulence modelling, while sand phase is modelled by a first order model through sand mass conservation, including the effect of advection by wind, sedimentation by gravity, and diffusion induced by sand particles collision at the wall. The progressive sand sedimentation occurring around the railway body is extrapolated depending on the value of the wind-sand interface velocity. This allows to assess wind flow, sand transport and sand sedimentation around the whole railway body. In particular, the resulting local wind flow and sand sedimentation occurring in correspondence of the track allow to identify the zones upwind and close downwind the upwind rail as the most prone to sand sedimentation and then properly set injection surfaces for sand particles and inlet boundary conditions as input for the following micro-scale simulations.

At the micro-scale, sand particles transport is modelled by means of three-dimensional Eulerian–Lagrangian computational simulations. RANS turbulence modelling is adopted for the wind phase, while the sand phase is modelled by Lagrange Multiphase Method in order to explicitly model the trajectory of particles subjected to advection by turbulent wind, sedimentation by gravity and lift by shear. The high-speed running train is modelled through the set-up of moving wall no-slip boundary conditions at ground. The resulting sand particles dispersion around the rolling stock components allow to assess the windblown sand action on the running train components in terms of both sand particles impact and infiltration. In particular, most of the sand particles impacts the rolling stock in the underfloor area. However, the crosswind induced vortex may cause their progressive lifting moving to the rear of the train leading to the eventual infiltration inside the heating, ventilation and air conditioning system.

In the wake of this wide and novel multi-physics multi-scale modelling approach, we suggest the following research perspectives. First, one of the advantages of the presented modelling framework is its modularity, i.e. different scale-modelling approaches can be adopted for each scale. As a result, the robustness of the model can be investigated by varying e.g. model constants, turbulence modelling of wind flow carrying phase and sand transported phase first/second order modelling approaches. Secondly, given the probabilistic assessment of the incoming sand drift, the proposed modelling approach can be adapted to obtain a resulting probabilistic windblown sand action. This could be achieved by uncertainty propagation modelling approaches commonly adopted in CWE (e.g. García-Sánchez and Gorlé, 2018). Thirdly, the effect induced by sand bed morphology could be investigated in micro-scale simulations to assess the effect induced on the windblown sand flow around the rolling stock, if any. Fourthly, in a design perspective, the study highlights how such a modelling approach can be adopted within the conceptual design and performance assessment of SMMs. Depending on the windblown sand transport scale, the modelling approach can be easily implemented to assess the performance of different SMM design solutions, but also to predict sand removal maintenance frequencies. In particular, the SMM design solutions shall be modelled within the part of the model related to the windblown sand transport scale that is mostly affected by the implementation of the SMM.

CRediT authorship contribution statement

Manuel Gageik: Methodology, Investigation, Formal analysis, Software, Visualization, Writing – review & editing. **Carlos-José Rodriguez Ahlert:** Methodology, Investigation, Formal analysis, Software, Visualization, Writing – review & editing. **Nicolas Coste:** Methodology, Investigation, Formal analysis, Software, Visualization, Writing – review & editing. **Lorenzo Raffaele:** Conceptualization, Investigation, Formal analysis, Methodology, Visualization, Writing – original draft, Writing – review & editing.

Declaration of competing interest

The authors declare that they have no known competing financial interests or personal relationships that could have appeared to influence the work reported in this paper.

Data availability

The data that has been used is confidential.

Acknowledgements

The study has been developed in the framework of the joint research and development activity carried out by SIEMENS Mobility GmbH (https://www.mobility.siemens.com/global/en.html) and Windblown Sand Modelling and Mitigation (WSMM, https://www.polito.it/WSMM/) joint research, development and consulting group established between Politecnico di Torino and Optiflow Company. This study was jointly carried in the framework of the research project PROtection Technologies from Eolian Events for Coastal Territories (PROTEECT, http://www.proteect.polito.it/) within the Ministerial Decree no. 1062/2021 and received funding from the FSE REACT-EU - PON Ricerca e Innovazione 2014–2020. This manuscript reflects only the authors' views and opinions, neither the European Union nor the European Commission can be considered responsible for them. This study was jointly carried out within the RETURN Extended Partnership and received funding from the European Union Next-GenerationEU

(National Recovery and Resilience Plan – NRRP, Mission 4, Component 2, Investment 1.3 – D.D. 1243 2/8/2022, PE0000005 - SPOKE TS2 Multi Risk Resilience of Critical Infrastructures). The Authors thank the other members of the WSMM group for the inspiring insight and fruitful discussion about the topic of the study.

References

Ali, I., Rüter, A., Rodriguez Ahlert, C., 2016. Numerical investigation on the embankment configuration for cross wind stability of ICE3. In: The Aerodynamics of Heavy Vehicles III: Trucks, Buses and Trains. http://dx.doi.org/10.1007/978-3-540-44419-0.

Bagheri, G., Bonadonna, C., 2016. On the drag of freely falling non-spherical particles. Powder Technol. 301, 526–544. http://dx.doi.org/10.1016/j.powtec.2016.06.015.

Barchyn, T.E., Hugenholtz, C.H., 2011. Comparison of four methods to calculate aeolian sediment transport threshold from field data: Implications for transport prediction and discussion of method evolution. Geomorphology 129, 190–203. http://dx.doi.org/10.1016/j.geomorph.2011.01.022.

Blocken, B., Stathopoulos, T., Carmeliet, J., 2007. CFD simulation of the atmospheric boundary layer: Wall function problems. Atmos. Environ. 41, 238–252. http://dx.doi.org/10.1016/j.atmosenv.2006.08.019.

Bruno, L., Coste, N., Mannini, C., Mariotti, A., Patruno, L., Schito, P., Vairo, G., 2023. Codes and standards on computational wind engineering for structural design: State of art and recent trends. Wind Struct. 37, 133–151. http://dx.doi.org/10.12989/was.2023.37.2.133.

Bruno, L., Fransos, D., 2015. Sand transverse dune aerodynamic: 3d coherent flow structures from a computational study. J. Wind Eng. Ind. Aerodyn. 147, 291–301. http://dx.doi.org/10.1016/j.jweia.2015.07.014.

Bruno, L., Fransos, D., Lo Giudice, A., 2018a. Solid barriers for windblown sand mitigation: Aerodynamic behavior and conceptual design guidelines. J. Wind Eng. Ind. Aerodyn. 173, 79–90. http://dx.doi.org/10.1016/j.jweia.2017.12.005.

Bruno, L., Horvat, M., Raffaele, L., 2018b. Windblown sand along railway infrastructures: A review of challenges and mitigation measures. J. Wind Eng. Ind. Aerodyn. 177, 340–365. http://dx.doi.org/10.1016/j.jweia.2018.04.021.

Cebeci, T., Bradshaw, P., 1977. Momentum Transfer in Boundary Layers. Washington DC Hemisphere Publishing Corp NY McGraw-Hill Book Co.

Cheng, J., Jiang, F., Xue, C., Xin, G., Li, K., Yang, Y., 2015. Characteristics of the disastrous wind-sand environment along railways in the Gobi area of Xinjiang, China. Atmos. Environ. 102, 344–354. http://dx.doi.org/10.1016/j.atmosenv.2014.12.018.

Clift, R., Gauvin, W.H., 1971. Motion of entrained particles in gas streams. Can. J. Chem. Eng. 49, 439–448. http://dx.doi.org/10.1002/cjce.5450490403.

EN 14067-6, 2018. Railway applications – aerodynamics. Part 6: Requirements and test procedures for cross wind assessment.

EN 1991-1-4, 2005. Eurocode 1: Actions on structures - part 1-4: General actions - wind actions - en 1991-1-4.

Faccoli, M., Petrogalli, C., Lancini, M., Ghidini, A., Mazzù, A., 2018. Effect of desert sand on wear and rolling contact fatigue behaviour of various railway wheel steels. Wear 396-397, 146–161. http://dx.doi.org/10.1016/j.wear.2017.05.012.

Fish, J. (Ed.), 2010. Multiscale Methods: Bridging the Scales in Science and Engineering. Oxford University Press.

Formaggia, L., Gerbeau, J., Nobile, F., Quarteroni, A., 2001. On the coupling of 3d and 1d Navier-Stokes equations for flow problems in compliant vessels 191. pp. 561–582. http://dx.doi.org/10.1016/S0045-7825(01)00302-4.

Fryberger, S., Dean, G., 1979. A study of global sand seas. Chapter Dune forms and wind regime. pp. 137–155.

García-Sánchez, C., Gorlé, C., 2018. Uncertainty quantification for microscale CFD simulations based on input from mesoscale codes. J. Wind Eng. Ind. Aerodyn. 176, 87–97. http://dx.doi.org/10.1016/j.jweia.2022.105109.

Gosman, A., Loannides, E., 1983. Aspects of computer simulation of liquid-fueled combustors 7. pp. 482–490. http://dx.doi.org/10.2514/3.62687.

Hersbach, H., et al., 2020. The ERA5 global reanalysis 146. pp. 1999–2049. http://dx.doi.org/10.1002/qj.3803.

Ho, T.D., Valance, A., Dupont, P., El Moctar, A.O., 2011. Scaling laws in Aeolian sand transport. Phys. Rev. Lett. 106, 094501. http://dx.doi.org/10.1103/PhysRevLett.106.094501.

Horvat, M., Bruno, L., Khris, S., 2021. CWE study of wind flow around railways: Effects of embankment and tracksystem on sand sedimentation. J. Wind Eng. Ind. Aerodyn. 208, 104476. http://dx.doi.org/10.1016/j.jweia.2020.104476.

Horvat, M., Bruno, L., Khris, S., 2022. Receiver sand mitigation measures along railways: CWE-based conceptual design and preliminary performance assessment. J. Wind Eng. Ind. Aerodyn. 228, 105109. http://dx.doi.org/10.1016/j.jweia.2022.105109.

Horvat, M., Bruno, L., Khris, S., Raffaele, L., 2020. Aerodynamic shape optimization of barriers for windblown sand mitigation using CFD analysis. J. Wind Eng. Ind. Aerodyn. 197, 104058. http://dx.doi.org/10.1016/j.jweia.2019.104058.

Iversen, J.D., Rasmussen, K.D., 1994. The effect of surface slope on saltation threshold. Sedimentology 41, 721–728. http://dx.doi.org/10.1111/j.1365-3091.1994.tb01419.x.

Kang, L., Liejin, G., 2006. Eulerian–Lagrangian simulation of aeolian sand transport 162. pp. 111–120. http://dx.doi.org/10.1016/j.powtec.2005.12.002.

Kok, J.F., Parteli, E.J.R., Michaels, T.I., Karam, D.B., 2012. The physics of wind-blown sand and dust. Rep. Progr. Phys. 75, 106901. http://dx.doi.org/10.1088/0034-4885/75/10/106901.

Launder, B.E., Spalding, D.B., 1974. The numerical computation of turbulent flows. Comput. Methods. Appl. Mech. Eng. 3, 269–289.

Lettau, K., Lettau, H., 1978. Experimental and Micro-Meteorological Field Studies of Dune Migration. Technical Report 101, pp. 110–147, Exploring the World' s Driest Climate (IES Report, 101, 110–147).

Liu, B., Qu, J., Zhang, W., Qian, G., 2011. Numerical simulation of wind flow over transverse and pyramid dunes. J. Wind Eng. Ind. Aerodyn. 99 (879), http://dx.doi.org/10.1016/j.jweia.2011.06.007.

Lo Giudice, A., Nuca, R., Preziosi, L., Coste, N., 2019. Wind-blown particulate transport: A review of computational fluid dynamics models. Math. Eng. 1, 508–547. http://dx.doi.org/10.3934/mine.2019.3.508.

Lo Giudice, A., Preziosi, L., 2020. A fully Eulerian multiphase model of windblown sand coupled with morphodynamic evolution: Erosion, transport, deposition, and avalanching. Appl. Math. Model 79, 68–84. http://dx.doi.org/10.1016/j.apm.2019.07.060.

Lopes, A., Oliveira, L., Pinto, J., 2013. Numerical simulation of sand dune erosion 13. pp. 145–168. http://dx.doi.org/10.1016/j.powtec.2005.12.002.

Menter, F.R., Kuntz, M., Langtry, R., 2003. Ten years of industrial experience with the SST turbulence model. In: Hanjalić, K., Nagano, Y., Tummers, J. (Eds.), Turbulence Heat and Mass Transfer 4: Proceedings of the Fourth International Symposium on Turbulence, Heat and Mass Transfer, Antalya, Turkey, 12-17 October, 2003. Begell House., p. 1208.

Narteau, C., Zhang, D., Rozier, O., Claudin, P., 2009. Setting the length and time scales of a cellular automaton dune model from the analysis of superimposed bed forms 114. p. F03006. http://dx.doi.org/10.1029/2008JF001127.

Newton, I., 1687. Philosophiae naturalis principia mathematica.

Nickling, W.G., 1988. The initiation of particle movement by wind. Sedimentology 35, 499–511. http://dx.doi.org/10.1111/j.1365-3091.1988.tb01000.x.

Paz, C., Suárez, C., Concheiro, M., 2015. Numerical study of the impact of windblown sand particles on a high-speed train. J. Wind Eng. Ind. Aerodyn. 145, 87–93. http://dx.doi.org/10.1016/j.jweia.2015.06.008.

Preziosi, L., Fransos, D., Bruno, L., 2015. A multiphase first order model for non-equilibrium sand erosion, transport and sedimentation. Appl. Math. Lett. 45, 69–75. http://dx.doi.org/10.1016/j.aml.2015.01.011.

Pye, K., Tsoar, H., 2009. Aeolian Sand and Sand Dunes. Springer, http://dx.doi.org/10.1007/978-3-540-85910-9.

Raffaele, L., Bruno, L., 2019. Windblown sand action on civil structures: Definition and probabilistic modelling. Eng. Struct. 178, 88–101. http://dx.doi.org/10.1016/j.engstruct.2018.10.017.

Raffaele, L., Bruno, L., 2020. Windblown sand mitigation along railway megaprojects: A comparative study. Struct. Eng. Int. 30, 355–364. http://dx.doi.org/10.1080/10168664.2020.1714530.

Raffaele, L., Bruno, L., Fransos, D., Pellerey, F., 2017. Incoming windblown sand drift to civil infrastructures: A probabilistic evaluation. J. Wind Eng. Ind. Aerodyn. 166, 37–47. http://dx.doi.org/10.1016/j.jweia.2017.04.004.

Raffaele, L., Bruno, L., Pellerey, F., Preziosi, L., 2016. Windblown sand saltation: A statistical approach to fluid threshold shear velocity. Aeolian Res. 23, 79–91. http://dx.doi.org/10.1016/j.aeolia.2016.10.002.

Raffaele, L., Bruno, L., Sherman, D.J., 2020. Statistical characterization of sedimentation velocity of natural particles. Aeolian Res. 44, 100593. http://dx.doi.org/10.1016/j.aeolia.2020.100593.

Raffaele, L., Bruno, L., Wiggs, G.F., 2018. Uncertainty propagation in aeolian processes: From threshold shear velocity to sand transport rate. Geomorphology 301, 28–38. http://dx.doi.org/10.1016/j.geomorph.2017.10.028.

Raffaele, L., Coste, N., Gertjan, G., 2022. Life-cycle performance and cost analysis of sand mitigation measures: Toward a hybrid experimental-computational approach. J. Struct. Eng. 148, http://dx.doi.org/10.1061/(ASCE)ST.1943-541X.0003344.

Raffaele, L., Glabeke, G., van Beeck, J., 2023. Wind sand tunnel experiment on the windblown sand transport and sedimentation over a two dimensional sinusoidal hill. Wind Struct. 36, 75–90. http://dx.doi.org/10.12989/was.2023.36.2.075.

Raffaele, L., van Beeck, J., Bruno, L., 2021. Wind-sand tunnel testing of surface-mounted obstacles: Similarity requirements and a case study on a Sand Mitigation Measure. J. Wind Eng. Ind. Aerodyn. 214, 104653. http://dx.doi.org/10.1016/j.jweia.2021.104653.

Richards, P., Norris, S., 2011. Appropriate boundary conditions for computational wind engineering models revisited. J. Wind Eng. Ind. Aerodyn. 99, 257–266. http://dx.doi.org/10.1016/j.jweia.2010.12.008.

Riksen, M.J., Goossens, D., Huiskes, H., Krol, J., Slim, P., 2016. Constructing notches in foredunes: Effect on sediment dynamics in the dune hinterland. Geomorphology 15, 340–352. http://dx.doi.org/10.1016/j.geomorph.2015.10.021.

Rodi, W., 1991. Experience with two-layer models combining the k-epsilon model with a one-equation model near the wall. http://dx.doi.org/10.2514/6.1991-216.

Saffman, P., 1965. Lift on a small sphere in a slow shear flow. J. Fluid Mech. 22 (385), http://dx.doi.org/10.1017/S0022112065000824.

Shao, Y., 2008. Physics and Modelling of Wind Erosion. Springer, http://dx.doi.org/10.1007/978-1-4020-8895-7.

Shih, T., Liou, W., Shabbir, A., Yang, Z., Zhu, J., 1994. A New K-Epsilon Eddy Viscosity Model for High Reynolds Number Turbulent Flows: Model Development and Validation. Technical Report. NASA Technical Memorandum, No. CMOTT-94-6.

Sim, J., Woo, S., Yook, S., Kim, J., Bae, G., Oh, S., 2018. Baffle dust collector for removing particles from a subway tunnel during the passage of a train 32. pp. 1415–1421. http://dx.doi.org/10.1007/s12206-018-0245-2.

Stokes, G.G., 1851. On the Effect of the Internal Friction of Fluids on the Motion of Pendulum, vol. 9, Pitt Press, Cambridge.

Sweby, P.K., 1984. High resolution schemes using flux limiters for hyperbolic conservation laws. SIAM J. Numer. Anal. 21, 995–1011.

Zakeri, J.A., Esmaeili, M., Mosayebi, S., Abbasi, R., 2012. Effects of vibration in desert area caused by moving trains. J. Mod. Transp. 20, 16–23. http://dx.doi.org/10.1007/BF03325772.